

# Advancing the Velocity Gradient Technique: Using Gradient Amplitudes and Handling Thermal Broadening

Ka Ho Yuen<sup>1</sup> and Alex Lazarian<sup>1,2</sup>

Department of Astronomy, University of Wisconsin-Madison, Madison, WI 53706 USA; kyuen@astro.wisc.edu, alazarian@facstaff.wisc.edu

2 Korea Astronomy and Space Science Institute, Daejeon 34055, Republic of Korea

Received 2020 January 27; revised 2020 April 26; accepted 2020 May 12; published 2020 July 24

### **Abstract**

The recent development of the velocity gradient technique allows observers to map magnetic field orientations and magnetization using the direction of velocity gradients. Aside from the directions, amplitudes of velocity gradients also contain valuable information about the underlying properties of magnetohydrodynamic (MHD) turbulence. In this paper, we explore what physical information is contained in the amplitudes of velocity gradients and discuss how this information can be used to diagnose properties of turbulence in both diffuse and self-gravitating interstellar media. We identify the relations between amplitudes of both intensity and velocity centroid gradients and the sonic Mach number  $M_s$ , and they are consistent with the theory's predictions. We test the robustness of the method and discuss how to utilize the amplitudes of gradients into self-gravitating media. To extend the velocity gradient technique, we also discuss the usage of amplitude method to position–position–velocity space as a possible way to retrieve the velocity channel maps before the contamination of thermal broadening. We discuss that the velocity gradient technique with these advancements could potentially give a significantly more accurate statistical insight into the properties of magnetized turbulence.

Unified Astronomy Thesaurus concepts: Interstellar medium (847); Interstellar magnetic fields (845); Interstellar dynamics (839)

#### 1. Introduction

Turbulence is ubiquitous in astrophysical environments. Magnetohydrodynamic (MHD) turbulence plays a very important role in various astrophysical phenomena (see Larson 1981; Armstrong et al. 1995; Biskamp 2003; Elmegreen & Scalo 2004; Chepurnov & Lazarian 2010), including star formation (see Mac Low & Klessen 2004; McKee & Ostriker 2007; Fissel et al. 2016), propagation and acceleration of cosmic rays (see Jokipii 1966; Yan & Lazarian 2008), and regulating heat and mass transport between different interstellar medium (ISM) phases (Green 1993; Deshpande et al. 2000; Dickey et al. 2001; Lazarian & Pogosyan 2004, 2006; Begum et al. 2006; Khalil et al. 2006; Padoan et al. 2006 see Draine 2009 for the list of the phases). Our understanding of MHD turbulence has been significantly improved owing to the establishment of the anisotropic scaling law (Goldreich & Sridhar 1995), the quantitative description of turbulent reconnection that is part and parcel of the MHD cascade (Lazarian & Vishniac 1999), and numerical studies that tested the theoretical ideas (Cho & Vishniac 2000; Maron & Goldreich 2001; Cho & Lazarian 2002, 2003; Kowal et al. 2009; Kowal & Lazarian 2010). A detailed discussion of the present understanding of MHD turbulence can be found in Beresnyak & Lazarian (2019).

Supported by the advancement of the MHD turbulence theory, the idea of using spectroscopic velocity gradients to trace magnetic field, namely, the velocity gradient technique (VGT; González-Casanova & Lazarian 2017; Yuen & Lazarian 2017a, 2017b; Lazarian & Yuen 2018a), was recently proposed and applied to observation data including galactic H I and self-gravitating molecular clouds. The recent development of VGT allows the measurements of magnetic field orientations by probing the peak of the velocity gradient orientation histogram in a statistically well-sampled area (Yuen & Lazarian 2017a). The orientations of velocity gradients are

taken into account for tracing the direction of magnetic field in both diffuse (Yuen & Lazarian 2017a) and self-gravitating media (Yuen & Lazarian 2017b; Lazarian & Yuen 2018a) based on turbulence scaling with the concept of block averaging (Yuen & Lazarian 2017a). The VGT has demonstrated its capability to trace magnetic fields in different ISM phases. Similar techniques based on the structures of turbulence have also been developed previously (Esquivel & Lazarian 2005; Heyer et al. 2008, 2009), but the method of gradients was shown to be better in comparison to them (Yuen et al. 2018). In some regimes of turbulence (see Beresnyak et al. 2005; Kowal et al. 2007), the turbulence velocity imprints its statistics on density. In this situation, intensity gradients (IGs) can also be used to trace magnetic field as shown in Lazarian & Yuen (2018a). The combined used of VCG and IG can also provide an extra physical gauge in both self-gravitating and shock regions (Yuen & Lazarian 2017b) and has been applied successfully to observational data (Hu et al. 2019b, 2019c).

We would like to note that the aforementioned IG technique, which is an offshoot of velocity gradient research, should be distinguished from the Histograms of Relative Orientation (HRO) technique (Soler et al. 2013; Soler & Hennebelle 2017; see also Hu et al. 2019a for a comparison between IG and HRO). Unlike the IGs under the block-averaging approach in Yuen & Lazarian (2017a), HRO is not a tool aimed at tracing the directions of magnetic field but is used to study the relative orientation of gradients and polarization statistically as a function of the column density (see Hu et al. 2019a).

The previous works on gradient technique mostly focus on the direction of the gradients of an observable (intensity, centroid, velocity channel) within a statistical region of interest. Recently, Lazarian et al. (2018) showed that the dispersion of velocity gradients in a sampling block is related to the local magnetization in the diffuse media. The statistics of gradient amplitudes in the framework of VGT and IGs have been

addressed in Yuen & Lazarian (2017b) when considering the filtering of shocks in the statistical prediction of gradient orientations. It was also suggested in Lazarian et al. (2018) that amplitudes of gradients in a statistical region of interest could possibly reflect the compressible nature of turbulence. However, a comprehensive discussion on the use of the gradient amplitudes similar to that for gradient orientations (e.g., Lazarian & Yuen 2018a) and dispersions (Lazarian et al. 2018) does not exist.

This paper continues our study of the utility of the gradient method in characterizing the physical properties of interstellar turbulence. In particular, we focus on the statistical properties of the gradient amplitudes of the observables. In this paper we focus mostly on obtaining estimates of  $M_s$  using gradient amplitudes, especially in the case of local interstellar media where the isothermal condition holds. We first discuss the theoretical expectations in Section 2, while our numerical setup is described in Section 3. We analyze the gradient amplitudes in Section 4 and discuss the robustness of the method in Section 5. We discuss one of the very important applications of the amplitude method that would allow removal of the thermal contributions from the observed position–position–velocity (PPV) cube in Section 7. We discuss our work in Section 8 and summarize our work in Section 9.

# 2. Statistics of Gradient Amplitudes Based on the Theory of MHD Turbulence

In our previous works, we already discussed how the directions (Lazarian & Yuen 2018a) and the dispersions (Lazarian et al. 2018) of gradients are related to the theoretical prediction of MHD turbulence anisotropy (Goldreich & Sridhar 1995; Lazarian & Vishniac 1999; Cho & Vishniac 2000; Maron & Goldreich 2001; see Brandenburg & Lazarian 2013 for a review and Beresnyak & Lazarian 2019 for a textbook). Readers can refer to our previous works on how the statistically averaged parameters in MHD turbulence are related to both gradient directions and dispersive quantities. Since Goldreich & Sridhar (1995) is a statistical theory describing the turbulence motion in the Eulerian frame, the respective analysis in the framework of gradients should also be performed statistically, either by obtaining averaged quantities spatially, temporally, or over ensembles. One realization of this statistical averaging is the sub-block averaging proposed in Yuen & Lazarian (2017a). In this paper, we will mainly focus on the prediction of the statistical properties of gradient amplitude based on the MHD theory of Goldreich & Sridhar (1995). Note that in the Goldreich & Sridhar (1995) framework Alfvén modes do not contribute to density fluctuations, which we discuss in Section 2.3.

# 2.1. Incompressible Limit

Based on the theory of *incompressible* MHD turbulence suggested by Goldreich & Sridhar (1995), the turbulent eddies are elongated along the magnetic field direction. In the original theory by Goldreich & Sridhar (1995) it is assumed that the latter direction is to be mean field direction. However, in fact, the turbulent eddies are aligned with the direction of local magnetic field. This follows from the ability of turbulent eddies to perform mixing motions that minimally bend magnetic fields. This ability comes from turbulent reconnection (Lazarian & Vishniac 1999) that allows magnetized turbulent eddies to change the magnetic topology within one eddy turnover time.

This dynamics of magnetized eddies in the local reference frame is proved numerically in Cho & Vishniac (2000) and Maron & Goldreich (2001). The mixing motions of an eddy induce a shearing force maximally perpendicular to the eddy's rotational axis. As this axis coincides with the local magnetic field direction, the 90°-rotated gradient of the absolute value of the eddy velocity aligns with the direction of magnetic field at the location of the eddy.

The Goldreich & Sridhar (1995) theory was formulated assuming that the turbulent injection velocity  $V_L$  is equal to the Alfvén velocity  $V_A$ . This means that the Alfvénic Mach number  $M_A = V_L/V_A$  was assumed to be 1. Realistic astrophysical settings present a variety of  $M_A$ , and the theory covering different magnetizations was formulated in Lazarian & Vishniac (1999). Below we reproduce the expressions derived there. For the case of sub-Alfvénic turbulence (Lazarian 2006), we consider only the strong turbulence with the scale  $l = 1/k < LM_A^2 = l_{\rm tr}$  since the weak turbulence usually contains very limited spatial range unless  $M_A \ll 1$ . Then, the velocity amplitude  $v_l$  at scale l would be

$$v_l \sim V_L \left(\frac{l_{\perp}}{L_{\rm inj}}\right)^{1/3} M_{\rm A}^{1/3},$$
 (1)

with  $L_{\rm inj}$  being the injection scale, while  $l_{\perp}$  represents the perpendicular (to magnetic field) length scale of the eddies. Since eddies are anisotropic along the magnetic field directions, we expect the gradients of velocities to be in the form of  $v_l/l_{\perp}$  as  $l_{\perp} \ll l_{\ll}$ . As a result, we would have a prediction of the velocity gradient amplitude of turbulence eddies of scale l:

$$\nabla v_l = \frac{v_l}{l_{\perp}} \sim \frac{V_L}{L_{\text{inj}}} \left(\frac{L_{\text{inj}}}{l_{\parallel}}\right)^{2/3} M_{\text{A}}^{1/3} \quad (M_{\text{A}} < 1, l < l_{\text{tr}}).$$
 (2)

Similar expressions could be obtained in the case of super-Alfvénic turbulence  $M_{\rm A}>1$  in the incompressible limit. In the case of super-Alfvénic turbulence, there is a transition scale  $l_{\rm A}=LM_{\rm A}^{-3}$ . When the length scale  $l>l_{\rm A}$ , the eddy is isotropic (i.e.,  $l=l_{\perp}=l_{\parallel}$ ), and the velocity gradient amplitude term would simply be

$$\nabla v_l \sim \frac{V_L}{L_{\rm inj}} \left(\frac{L_{\rm inj}}{l}\right)^{2/3} \quad (M_A > 1, l > l_A), \tag{3}$$

while in the case of  $l < l_{\rm A} = L M_{\rm A}^{-3}$ , the anisotropy of eddies still exists and follows the magnetic field line. Hence,  $l_{\perp} < l_{\parallel}$  and

$$\nabla v_l \sim \frac{V_L}{L_{\rm inj}} \left( \frac{L_{\rm inj}}{l_{\perp}} \right)^{2/3} \quad (M_{\rm A} > 1, \, l < l_{\rm A}).$$
 (4)

In simulations, the parameters  $V_L$  and  $L_{\rm inj}$  are given at the start of the turbulence driving and stay constant under temporal evolution. The three-dimensional velocity gradient amplitude is the sum of velocity gradient amplitudes from eddies of different scales, for which we would expect the smallest scale permissible in the simulation to dominate. As a result, we would have the simplified, easily memorable expression for the amplitudes of velocity gradients that we would use throughout

the whole paper:

$$\nabla v_l \propto l_{\perp}^{-2/3} \min(M_{\rm A}^{1/3}, 1).$$
 (5)

In incompressible turbulence, there should have been no density fluctuations  $\delta\rho$  since Alfvén modes do not induce such fluctuations. As a result, the density gradients are not considered in the incompressible limit of MHD turbulence.

# 2.2. Compressible Turbulence

In the case of compressible turbulence, three MHD modes arise, namely, the incompressible Alfvén mode and the two compressible modes called fast and slow modes. For magnetically dominated low- $\beta$  media, fast modes arise from the compression of magnetic field lines in its perpendicular directions, while slow modes are compression along the magnetic field lines. In the media dominated by gas pressure, or high- $\beta$  media, the fast modes are similar to sound waves and slow modes are density perturbations propagating along magnetic field directions. Cho & Lazarian (2002) showed that the driving of compressible modes from Alfvén modes is marginal, provided that either the external magnetic field or the gas pressure is sufficiently high. Since the Alfvén mode expressions are the same as what is derived above, below we shall follow the framework of Cho & Lazarian (2003) in deriving the relevant expressions of velocity and density gradient amplitudes for the two compressible MHD modes.

The methodology in deriving the velocity gradient amplitude  $\nabla v_l$  for eddies of scale l here follows from two expressions: (1) how the energy spectrum behaves,  $E(k) \propto k^{-p-1}$ , or  $E(l) \sim v_l^2 \propto l^p$  or  $l_\perp^p$  for some p, and (2) whether the system is anisotropic  $l_\parallel \propto l_\perp^q$  for some q. Then, the expected relation for velocity gradient amplitude would be  $\nabla v_l \sim l_\perp^{p/2-1}$  if q < 1 and  $\nabla v_l \sim l^{p/2-1}$  otherwise. For instance, if we have the Kolmogorov energy spectrum  $E(k) \sim k^{-5/3}$ , this would suggest that  $v_l^2 = E(l) \sim l^{2/3}$ , thus having the same power law as in Equation (1). Below we shall discuss the cases according to the plasma beta  $\beta = 2M_{\rm A}^2/M_{\rm S}^2$ , where  $M_{\rm S} = v_L/c_{\rm S}$  is the sonic Mach number and  $c_{\rm S}$  is the thermal speed.

If the turbulent flow is highly supersonic, a steeper velocity spectral slope of -2 is consistently seen in the simulations (Federrath et al. 2010; Kowal & Lazarian 2010) for all three modes, suggesting that  $\nabla v_{l,\mathrm{alf/slow/fast}} \propto l^{-1/2}$  in the highly supersonic regime.

For slow modes in the high- $\beta$  and mildly supersonic low- $\beta$  regime ( $M_S$  <= 2.3 as defined in Cho & Lazarian 2003), the velocity scaling relation follows completely from the Alfvén mode case, as a result of the dependence of velocity gradient amplitudes toward the length scale, and Mach numbers would follow what we derived from the previous subsection, i.e.,  $\nabla v_{l,\mathrm{slow}} \propto l^{-2/3}$ .

Fast modes do not have changes of the spectral behavior with respect to  $\beta$  as long as  $M_s$  is mildly small. It follows a spectrum of  $E_k \sim k^{-3/2}$  and isotropic in small scales  $k_\perp = k_\parallel$ . Therefore, we would expect the velocity gradient amplitude of the fast mode eddies to follow  $\nabla v_{l,\mathrm{fast}} \propto l^{-3/4}$ .

### 2.3. Density Gradient Amplitudes for Slow and Fast Modes

The density of the eddies at Fourier scale k = 1/l can also be written as, following Cho & Lazarian (2003),

$$|\rho_k| = \frac{\rho_0 \nu_k}{c} |\hat{k} \cdot \hat{\zeta}|,\tag{6}$$

where  $\rho_0$  is the mean density,  $\hat{\zeta}$  is the unit vector for the respective mode as listed in the Appendix of Cho & Lazarian (2003), and c is the respective sound speed for the MHD mode. From here we can write the (three-dimensional) density gradient amplitude as

$$\nabla \left( \frac{|\rho_l|}{\rho_0} \right) \sim \frac{\rho_l}{\rho_0 l} \sim \nabla v_l(c^{-1} \mathscr{F}^{-1} | \hat{\boldsymbol{k}} \cdot \hat{\boldsymbol{\zeta}} |), \tag{7}$$

where we still keep the dot product term in the Fourier space with the inverse Fourier transform operator  $\mathcal{F}^1$  to remind the reader that an inverse Fourier transform should be done after the dot product (Cho & Lazarian 2003, 2006). One can observe that the density gradient amplitude is simply the velocity gradient amplitude multiplied by two extra terms: the dot product term and the sound speed contribution. The dot product term and the sound speed have been derived previously in Cho & Lazarian (2003):

$$\nabla \left(\frac{|\rho_{l}|}{\rho_{0}}\right) \propto \nabla v_{l} M_{s} \quad (\beta \ll 1, \text{ slow modes})$$

$$\nabla \left(\frac{|\rho_{l}|}{\rho_{0}}\right) \propto \nabla v_{l} M_{A} \quad (\beta \ll 1, \text{ fast modes})$$

$$\nabla \left(\frac{|\rho_{l}|}{\rho_{0}}\right) \propto \nabla v_{l} M_{s}^{2} / M_{A} \quad (\beta \gg 1, \text{ slow modes})$$

$$\nabla \left(\frac{|\rho_{l}|}{\rho_{0}}\right) \propto \nabla v_{l} M_{s}^{2} \quad (\beta \gg 1, \text{ fast modes}). \tag{8}$$

The expectations of the dependence of mode gradient amplitudes are summarized in Table 1. The exact relation of how the velocity and density gradient amplitudes would be related to different physical parameters are subject to the ratio of the MHD modes in the environment. Cho & Lazarian (2002) suggested that Alfvén modes are usually predominant in interstellar media and fast modes are infinitesimal, suggesting that we could possibly only look at the Alfvén mode and slow mode dependence (Table 1) when considering the velocity and density gradient amplitudes, respectively.

# 2.4. Observational Diagnostics for Gradient Amplitudes

Since we do not observe the three-dimensional velocity and density gradient amplitudes in observation, it is necessary to discuss how the observables, namely, the column density (intensity)  $I = \int \rho dz$ , velocity centroid  $C = \int \rho v_z dz/I$ , and velocity channel maps, are expected to behave based on the discussion in the previous subsections. In the following we shall discuss first the intensity and centroid maps and postpone the discussion of channel map gradients to later sections.

Table 1
Predictions on the Dependence of Gradient Amplitudes as a Function of Length Scale l, Sonic Mach Number  $M_s$ , and Alfvénic Mach Number  $M_A$  for Different Regimes

	$\beta \ll 1, M_s < 1$			$\beta \gg 1$ , $M_s < 1$			$M_s \gg 1$
	Alfvén Mode	Slow Mode	Fast Mode	Alfvén Mode	Slow Mode	Fast Mode	All MHD Modes
$\nabla v_l$	$\propto l^{-2/3} \min(M_{\rm A}^{1/3}, 1)$	$\propto l^{-2/3}$	$\propto l^{-3/4}$	$\propto l^{-2/3} \min(M_{\rm A}^{1/3}, 1)$	$\propto l^{-2/3}$	$\propto l^{-3/4}$	$\propto l^{-1/2}$
$\nabla \left( \frac{\mid \rho_l \mid}{\rho_0} \right)$	N/A	$\propto l^{-2/3} M_s$	$\propto l^{-3/4}M_{\rm A}$	N/A	$\propto l^{-2/3}M_s^2/M_A$	$\propto l^{-3/4}M_s^2$	Follow Equation (8)

# 2.4.1. Relationship between the Two-dimensional and Threedimensional Gradient Amplitude Quantities

We first assume that the mean magnetic field is on the plane of sky and take the intensity gradient amplitude as an example. The quantity  $\nabla_{2\mathrm{D}}I = \int \nabla_{2\mathrm{D}}\rho dz$  suggests that (1) the semiminor axis  $\mathbf{1}_{\perp}$  lines on the plane of sky suggest that  $\nabla_{2\mathrm{D}}\rho = \nabla\rho$  and (2) the sign of the density gradient amplitudes along the line of sight follows a random walk. Assuming we have  $N = L_{\mathrm{los}}/L_{\mathrm{inj}}$  eddies along the line of sight in the stage of the injection, we would then have an estimation of intensity gradient amplitudes

$$\nabla_{2D}I \propto \nabla \rho L_{\rm inj} \sqrt{N},$$
 (9)

which suggests that the intensity gradient amplitude is proportional to the density gradient amplitudes with extra factors that would be a constant in time in simulations. If the mean magnetic field makes an angle of  $\theta$  to the line-of-sight magnetic field, then there would be an extra  $\cos \theta$  factor in Equation (9) owing to the conversion of  $\nabla_{2D}$  to  $\nabla_{3D}$ , i.e.,  $\nabla_{2D}I \propto \nabla \rho \cos \theta$ . However, as shown in Yuen & Lazarian (2020), the insertion of the  $\cos \theta$  in compensating the effect of line-of-sight angle is not correct. We can understand the argument by considering a magnetic field line with an inclination angle  $\theta$ . Conceptually, the magnetic field contains both the mean and the turbulent components, for which we can assume that the latter is perpendicular to the mean field. In the case when the mean field component is almost aligned with the line of sight, the observed magnetic field would be contributed mostly by the turbulent component of the magnetic field plus a small contribution from the mean field. If it happens that the Alfvénic Mach number is large enough, i.e., the turbulent-tomean magnetic field strength ratio is large, then the observed magnetic field on the plane of sky is larger than the expected strength computed by  $B \cos \theta$ . The same argument applies to all vector quantities, in particular, the intensity gradient amplitude as in Equation (9). From a similar argument in, we see that such an approximation formula in Equation (9) is correct only when  $\theta > 4 \tan^{-1}(M_A/\sqrt{3})$ .

The situation in velocity centroid is more complicated since there are two terms upon differentiation. Esquivel & Lazarian (2005) showed that the velocity centroid is a proper measure of velocities. However, upon planar differentiation how the density and velocity gradient terms would contribute relatively is unknown and requires more substantial research. From previous numerical work on VGT (Lazarian & Yuen 2018a), it is apparent that the velocity weighting in the calculation of velocity centroids increases the velocity nature in terms of the structures, regardless of the normalization constant. Therefore,

we would expect the velocity centroid to be "more velocity like" (see Kandel et al. 2017).

Velocity channels (Lazarian & Pogosyan 2000, 2004) are even more complicated than velocity centroids because (1) the decreased velocity channel width would then increase the velocity weighting in the channel map and (2) the increase of thermal broadening washes away the velocity nature in the channel map. Both factors depend on the spectra of densities and velocities, as well as the sonic Mach number of the interstellar medium. It is expected that in the case of high sonic Mach number, the shocks, together with the velocity ambient map, would be more apparent in the velocity channel map (Yuen & Lazarian 2017a; Lazarian & Yuen 2018a). A suitable thermal deconvolution algorithm is required if sonic Mach number is too low (see Section 7).

### 2.4.2. Proper Statistical Averaging in Observations

As discussed above, some sort of statistical averaging is required to make the prediction of MHD theory (Table 1) applicable. A straightforward statistical measure would be to compute the mean and dispersion of the gradient amplitudes within a large enough statistical sampling area. We take the case of velocity gradient amplitude as an example since the respective observables are directly proportional to the velocity gradient amplitudes as shown in previous subsections. From Table 1 we can safely assume  $\nabla v \propto l^a M_A^b$  for some number a,b. Given an averaging volume V, the sonic and Alfvénic Mach numbers are computed already. The mean and dispersion of velocity gradient amplitude are simply the mean and the dispersion of the respective length scale mean and dispersion times the relevant Mach numbers, i.e.,

$$\langle \nabla v_l \rangle_l \propto \langle l^a \rangle_l M_A^b \sigma_{\nabla v_l} \sim \sigma_{l^a} M_A^b;$$
 (10)

therefore, using these simple statistical quantities would allow observers to trace the sonic and Alfvénic pre-factor, respectively.

As a summary of the current section, we derive the incompressible three-dimensional velocity gradient amplitude relation based on the MHD theory (Section 2.1). Based on that, we further proceed in deriving the velocity gradient amplitude relation for different modes in compressible turbulence (Section 2.2), for which we found that the Alfvén mode would be the dominant term in the gradient amplitudes of velocities. The respective density gradient amplitude relations for slow and fast modes are derived in Section 2.3, and we predict that the slow modes would then dominate the fluctuation of density gradient amplitudes. In Section 2.4 we connect the gradient amplitudes of two-dimensional observables to the threedimensional counterparts and further show that the simple statistical measures of intensity and velocity gradient amplitudes would allow observers to measure the Mach numbers as listed in Table 1. From our deviation in Table 1, it is apparently

easier to explore the relation between the gradient amplitude of the observables and  $M_s$  since the dependence of the gradient amplitude of the observables on  $M_A$  is highly nonlinear and mode dependent.

#### 3. Method

The numerical data cubes are obtained by 3D MHD simulations that are from a single-fluid, operator-split, staggered-grid MHD Eulerian code ZEUS-MP/3D to set up a three-dimensional, uniform turbulent medium. Most of our simulations are isothermal with  $T=10\,\mathrm{K}$ , but some of them are adiabatic by assuming  $P\propto \rho^{5/3}$  to mimic the properties of the warm neutral media (Kritsuk et al. 2017; see also the Appendix). To simulate part of the interstellar cloud, periodic boundary conditions are applied. We inject turbulence solenoidally.

For our controlling simulation parameters, various Alfvénic Mach numbers  $M_A = V_{\rm inj}/V_A$  and sonic Mach numbers  $M_s = V_{\rm inj}/V_s$  are employed, where  $V_{\rm inj}$  is the injection velocity, while  $V_A$  and  $V_s$  are the Alfvén and sonic velocities, respectively, which are listed in Table 2. For the case of  $M_A < M_s$ , it corresponds to the simulations of turbulent plasma with thermal pressure smaller than the magnetic pressure, i.e., plasma with low confinement coefficient  $\beta/2 = V_s^2/V_A^2 < 1$ . In contrast, the case  $M_A > M_s$  corresponds to the magnetic-pressure-dominated plasma with high confinement coefficient  $\beta/2 > 1$ .

Further, we refer to the simulations in Table 2 by their model name. For example, the figures with model name indicate which data cube was used to plot the corresponding figure. The selected ranges of  $M_s$ ,  $M_A$ , and  $\beta$  are determined by possible scenarios of astrophysical turbulence from very subsonic to supersonic cases.

The raw data from simulation cubes are converted to synthetic maps for our gradient studies. The normalized velocity centroid  $C(\mathbf{R})$  in the simplest case<sup>5</sup> is defined as

$$C(\mathbf{R}) = I^{-1} \int \rho_{\nu}(\mathbf{R}, \nu) \nu d\nu,$$
  

$$I(\mathbf{R}) = \int \rho_{\nu}(\mathbf{R}, \nu) d\nu,$$
(11)

where  $\rho_{\nu}$  is density of the emitters in the PPV space,  $\nu$  is the velocity component along the line of sight, and R is the 2D vector in the pictorial plane. The integration is assumed to be over the entire range of  $\nu$ . Naturally, I(R) is the emission intensity. The C(R) is also an integral of the product of velocity and line-of-sight density, which follows from a simple transformation of variables (see Lazarian & Esquivel 2003).

Table 2
Description of MHD Simulation Cubes, Some of Which Have Been Used in the Series of Papers about VGT (Yuen & Lazarian 2017a, 2017b; Lazarian & Yuen 2018a, 2018b)

Model	$M_S$	$M_{\rm A}$	$\beta = 2M_{\rm A}^2/M_{\rm S}^2$	Resolution
m0	5.73	0.22	0.0029	$360^{3}$
m1	5.79	0.42	0.011	$360^{3}$
m2	5.69	0.61	0.023	$360^{3}$
m3	5.46	0.82	0.045	$360^{3}$
m4	5.50	1.01	0.067	$360^{3}$
m5	5.51	1.19	0.093	$360^{3}$
m6	5.45	1.38	0.13	$360^{3}$
m7	5.41	1.55	0.16	$360^{3}$
m8	5.41	1.67	0.19	$360^{3}$
m9	5.40	1.71	0.20	$360^{3}$
Ms0.4Ma0.04	0.41	0.04	0.02	480 <sup>3</sup>
Ms0.8Ma0.08	0.92	0.09	0.02	$480^{3}$
Ms1.6Ma0.16	1.95	0.18	0.02	$480^{3}$
Ms3.2Ma0.32	3.88	0.35	0.02	$480^{3}$
Ms6.4Ma0.64	7.14	0.66	0.02	$480^{3}$
Ms0.4Ma0.132	0.47	0.15	0.22	$480^{3}$
Ms0.8Ma0.264	0.98	0.32	0.22	$480^{3}$
Ms1.6Ma0.528	1.92	0.59	0.22	$480^{3}$
Ms0.4Ma0.4	0.48	0.48	2.0	$480^{3}$
Ms0.8Ma0.8	0.93	0.94	2.0	$480^{3}$
Ms0.132Ma0.4	0.16	0.49	18	$480^{3}$
Ms0.264Ma0.8	0.34	1.11	18	$480^{3}$
Ms0.04Ma0.4	0.05	0.52	200	$480^{3}$
Ms0.08Ma0.8	0.10	1.08	200	$480^{3}$
huge-0	6.17	0.22	0.0025	792 <sup>3</sup>
huge-1	5.65	0.42	0.011	$792^{3}$
huge-2	5.81	0.61	0.022	$792^{3}$
huge-3	5.66	0.82	0.042	$792^{3}$
huge-4	5.62	1.01	0.065	$792^{3}$
huge-5	5.63	1.19	0.089	792 <sup>3</sup>
huge-6	5.70	1.38	0.12	792 <sup>3</sup>
huge-7	5.56	1.55	0.16	792 <sup>3</sup>
huge-8	5.50	1.67	0.18	792 <sup>3</sup>
huge-9	5.39	1.71	0.20	$792^{3}$
h0-1200	6.36	0.22	0.00049	1200 <sup>3</sup>
h9-1200	10.79	1.26	0.0068	$1200^{3}$
e5r2	0.13	1.57	292	$1200^{3}$
e5r3	0.61	0.52	1.45	$1200^{3}$
e6r3	5.45	0.24	0.0039	$1200^{3}$
e7r3	0.53	1.31	12.22	$1200^{3}$
h0-1600	5.56	0.20	0.0026	$1600^{3}$
Ms0.2Ma0.2	0.2	0.2	2	480 <sup>3</sup>
Ms0.4Ma0.2	0.4	0.2	0.5	$480^{3}$
Ms4.0Ma0.2	4.0	0.2	0.005	$480^{3}$
Ms20.0Ma0.2	20.0	0.2	0.0002	$480^{3}$

**Note.**  $M_s$  and  $M_A$  are the rms values at each snapshot.

For constant density, C(R) is just a velocity averaged over the line of sight.

### 4. Gradient Amplitude Statistics in Numerical Simulations

Driven by the theoretical derivation from Section 2.3, it is very natural to consider the quantity  $\nabla I' = \nabla (I/\langle I \rangle)$  since the corresponding density gradient amplitude is in the form  $\nabla (\rho/\langle \rho \rangle)$ , which is obtained by the Sobel kernel. The mean

These simulations are the Fourier-space forced driving isothermal simulations. The choice of force stirring over the other popular choice of decaying turbulence is because only the former will exhibit the full characteristics of turbulence statistics (e.g., power law, turbulence anisotropy) extended from k=2 to a dissipation scale of 12 pixels in a simulation, and it matches with what we see in observations (e.g., Armstrong et al. 1995; Chepurnov & Lazarian 2010).

<sup>&</sup>lt;sup>4</sup> For isothermal MHD simulation without gravity, the simulations are scale-free. The two scale-free parameters  $M_A$ ,  $M_s$  determine all properties of the numerical cubes, and the resultant simulation is universal in the inertial range. That means that one can easily transform to whatever units as long as the dimensionless parameters  $M_A$ ,  $M_s$  are not changed.

Higher-order centroids are considered in Yuen & Lazarian (2017b), and they have  $v^n$ , e.g., with n = 2, in the expression of the centroid. Such centroids may have their own advantages. However, for the sake of simplicity we employ for the rest of the paper n = 1.

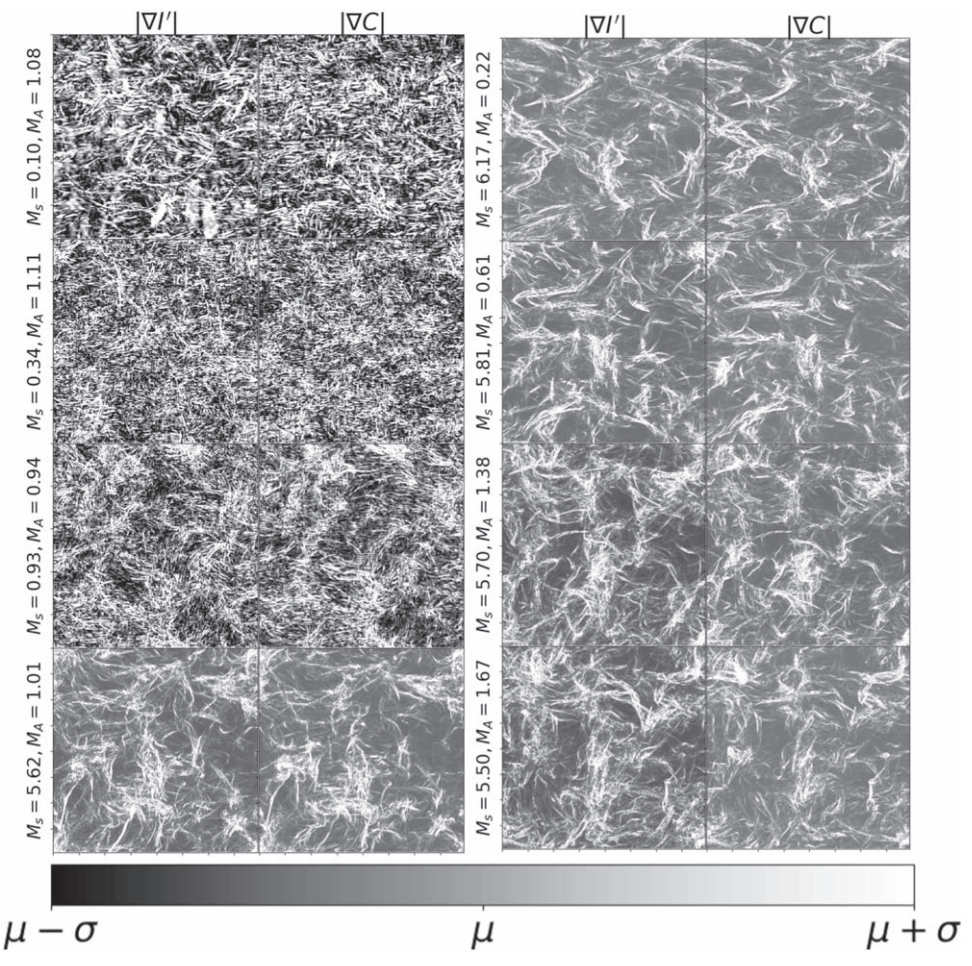


Figure 1. Visual illustrations of how  $M_s$  (left column) and  $M_A$  (right column) change gradients of intensities and gradients of centroids, i.e.,  $|\nabla I|$ ,  $|\nabla C|$ , which we study here. The color bar scales are the same for all plots, that the darkest color corresponds to the mean value minus the standard variation of the respective map, while the lightest color corresponds to the mean value plus the standard variation.

 $\mu$  and dispersion  $\sigma$  are then defined as

$$\mu = \langle |\nabla I'| \rangle$$

$$\sigma = \langle |\nabla I'|^2 \rangle - \mu^2,$$
(12)

for which we would compute the average over the whole intensity map. Notice that the gradient amplitudes have an inverse dependence on the length, for which in our code unit each  $\nabla$  operator is multiplied by a factor of  $n_x/10$  pc, where  $n_x$  is the resolution of the cubes.

We will first illustrate visually how the structures of gradient amplitudes are correlated with the dimensionless physical parameters. Figure 1 shows how  $|\nabla I'|$  and  $|\nabla C|$  behave when  $M_s$  (left column) and  $M_A$  (right column) change by keeping the other parameter approximately constant. The color scale in Figure 1 is set so that the darkest color always corresponds to  $\mu-\sigma$  and the lightest color always corresponds to  $\mu+\sigma$ . One could see that the structure of both gradient amplitudes becomes spatially thinner as  $M_s$  increases. We would then expect there to exist some correlation between  $|\nabla I'|$  and  $|\nabla C|$  with respect to the sonic Mach number  $M_s$ . Comparatively, the gradient amplitude maps for both intensity and centroid maps do not vary much in terms of the spatial width of the structures with respect to  $M_A$ .

Following the deviations from Section 2.3, we would expect the slow mode to dominate the intensity gradient amplitudes.

As a result,  $\nabla I' \propto M_s$  for  $\beta < 1$  and  $\propto M_s^2$  for  $\beta > 1$ , where we temporarily suppress the relation to  $M_A$  and the mode weights here. The left panel of Figure 2 shows the intensity gradient amplitude  $\nabla I' = \nabla (I/\langle I \rangle)$  as a function of the sonic Mach number  $M_s$  using the 45 isothermal simulations with different resolutions as we listed in Table 2. These data are prepared so that they contain variations of  $M_s$  and  $M_A$ . The variations are introduced since we would like to see how strongly the one parameter would interfere with the power-law behavior that we are seeking when we are comparing the  $\sigma_{\nabla I'}$  to the other parameter. We draw two auxiliary lines showing our predicted power laws from Table 1; one corresponds to the regime where  $\nabla I' \propto M_s$  when  $\beta \ll 1$ , while the other one corresponds to the regime with  $\nabla I' \propto M_s^2$  when  $\beta \to \infty$ . We could visually see that the theoretical expectation fairly fits the simulation data. Statistically both the part with  $\propto M_s$  and the part with  $\propto M_s^2$  have coefficients of determination of  $\sim 0.89$  and 0.96, respectively.

Readers should keep in mind that the deviations listed in Table 1 correspond to the extreme cases of  $\beta$  only. It is natural to have a different transitional power law when  $\beta \sim 1$ , as readers might be able to spot that already in the left panel of Figure 2. In fact, the intermediate regime has not been theoretically studied either in the framework of MHD turbulence, but it has very important astrophysical importance since observationally clouds with, e.g.,  $M_s \sim M_A \sim 1$  are not rare in lukewarm neutral media (despite that they have different

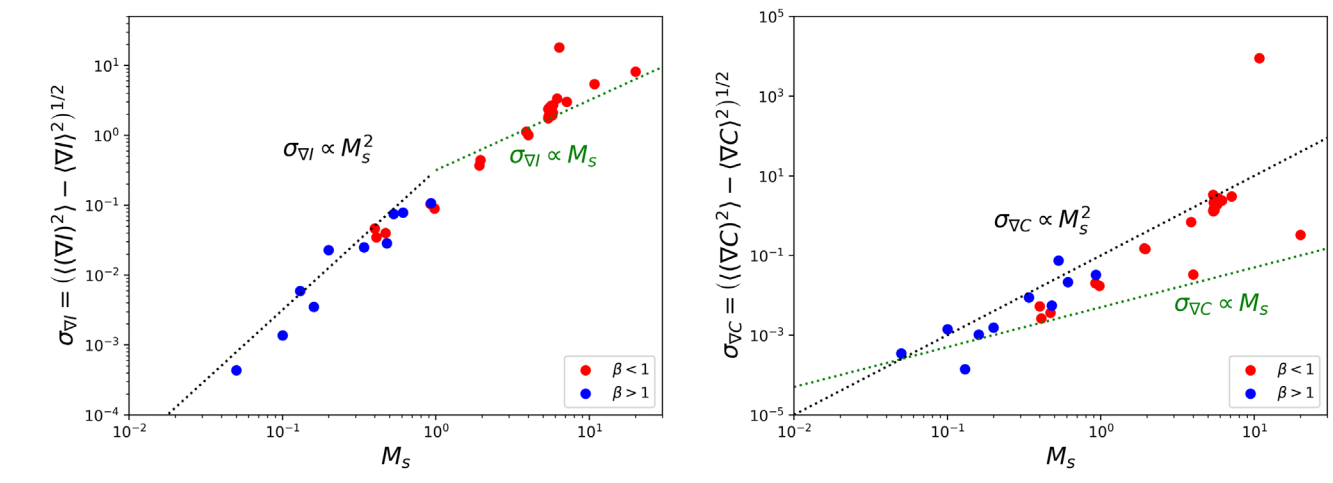


Figure 2. Intensity gradient amplitude  $\nabla I' = \nabla (I/\langle I \rangle)$  (left) and centroid gradient amplitude  $\nabla C$  (right) as a function of the sonic Mach number  $M_s$ . Due to the prediction in Table 1, we show the data with  $\beta > 1$  in blue and those with  $\beta < 1$  in red. We also draw two auxiliary lines (green:  $\infty M_s$ ; black:  $\infty M_s^2$ ) showing our predicted power laws.

thermal properties) or in the case of collapsing core (despite that gravity enhances the generation of growing slow and fast modes). Studies of gradient amplitudes in the intermediate regimes should be combined with the more popular tools like the N-PDF method (Burkhart & Lazarian 2012; Konstandin et al. 2012) for better accuracy.

The theory also expects variations due to the different weighting of MHD modes as  $\beta$  changes. For instance, in the case of  $\beta \ll 1$  and small  $M_s$ , slow modes would contribute to the 3D density gradient amplitude as  $\propto l^{-2/3}M_s$ , while that of fast modes as  $\propto l^{-3/4} M_{\rm A}$ . Similarly in the case of  $\beta \gg 1$  and small  $M_s$ , the corresponding power law is  $\propto l^{-2/3}M_s^2/M_A$  and  $\propto l^{-3/4} M_s^2$ , respectively, for slow and fast modes. When  $M_s$  is large, we expect to have no spatial dependence l in the power law. From Table 1 we see that (1) the Alfvén modes do not introduce any density fluctuations, so we can neglect it for the time being; (2) the contribution of slow modes to  $\nabla I$  is  $\propto M_s$ ; (3) the contribution of fast modes to  $\nabla I$  is  $\propto M_A$ ; and (4) the relative slow-to-fast mode energy ratio in our simulations with random driving at  $\beta < 1$  is roughly 3:1. With these factors taken into account, we can see that  $M_A$  is inevitably contributing to both  $\sigma_{\nabla I}$  and  $\sigma_{\nabla C}$  depending on the weighting of fast modes. Yet from the same argument, we see that the fast modes are subdominant in all of our simulations. In this scenario we expect that the slow-mode dependence (i.e.,  $\propto M_s$ ) would dominate over that of fast modes. The nonlinear effect that  $M_A$  has in the power law might affect the prediction of  $M_s$ using Table 1. In view of that, we prepared the two subsets of data "m0-m9" and "huge-0-huge-9," which carry fairly close  $M_s$  but a wide range of  $M_A$ , to see how  $M_A$  would change the predictions in Table 1. We divide standard variations of  $\nabla I'$  of these two sets of data and compare to the mean value of them, and we find that the standard deviation accounts for 14% and 6% only for the sets "m0-m9" and "huge-0-huge-9," respectively. Thus, we believe that  $M_A$  would be a less important factor compared to  $M_s$  as in the left panel of Figure 2.

We showed in Section 2.4 that the centroid gradient amplitude is not the ideal variable in obtaining the sonic Mach number owing to the composite product of density and velocity, making it difficult to isolate the effect of density from velocities in centroids. It would still be interesting to see

how the centroid gradient amplitude would behave as a function of sonic Mach number. Here we would expect that the velocity centroid would follow a power law to be an undetermined mixture of density and velocity power law as predicted from Table 1. As we see from Section 2.1, the three-dimensional velocity gradient amplitude relation (see, e.g., Equation (2)) does not carry a factor of  $M_s$ , meaning that the resultant centroid gradient amplitude term would solely come from the density contribution.

In the computation of velocity centroid, we would simply compute  $\sigma_{\nabla C} = (\langle (\nabla C)^2 \rangle - \langle \nabla C \rangle^2)^{1/2}$  instead of computing the  $\sigma_{\nabla C/\langle C \rangle}$ , since velocity terms do not require such a normalization as shown in Section 2. In the right panel of Figure 2 we show the variations of  $\sigma_{\nabla C}$  as a function of  $M_s$ . Due to the cumulative contribution of density and velocity terms, it is expected to have some power law that deviates from  $M_s$  or  $M_s^2$ . We can see that while the blue points are generally following the  $\propto M_s$  power law, the red data points exhibit a more scattered pattern. Yet the centroid gradient amplitude is shown to suffer from lesser influences from the line-of-sight angle effects, which we will discuss in Section 5.1.

### 5. Robustness of the Methods

# 5.1. The Angle between Magnetic Field and Line of Sight

In Section 2.4 we expect that the angle between the mean magnetic field and the line of sight would also be an important factor in affecting the computed gradient amplitude. While the turbulent eddies are anisotropic following the theoretical prediction in Goldreich & Sridhar (1995), it is shown (Burkhart et al. 2014; Yuen et al. 2018) that the correlation function anisotropy of velocity centroids drops significantly from anisotropic to merely isotropic as the relative angle  $\theta$  between the mean magnetic field  $\langle B \rangle$  and the line-of-sight directions decreases. Readers should be careful that the study performed in Section 4 has a mean magnetic field perpendicular to the line of sight, i.e.,  $\theta = 90^{\circ}$ .

To characterize how the relative angle  $\theta$  would change the result in Figure 2, we consider the following quantity that

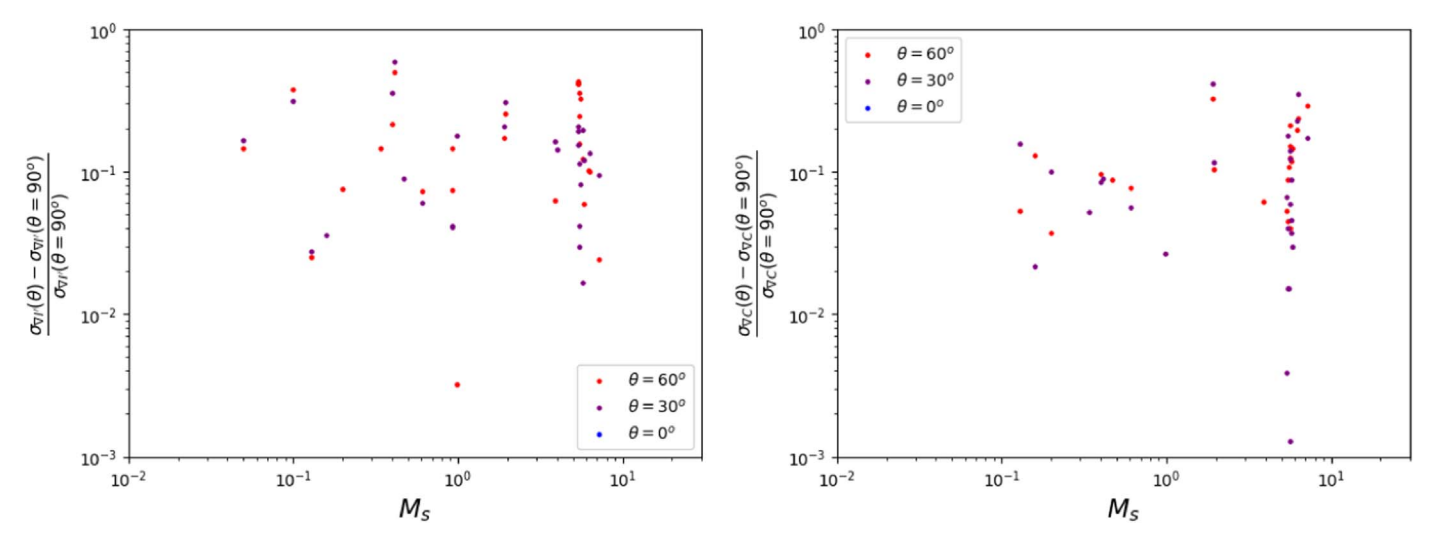


Figure 3. Fractional change (see Equation (13)) of both intensity gradient amplitude dispersion  $\sigma_{\nabla l'}$  (left) and the centroid gradient amplitude dispersion  $\sigma_{\nabla l'}$  (right) as functions of the relative angle  $\theta$  (in degrees) between the mean magnetic field  $\langle B \rangle$  and the line-of-sight directions (in the case of Figure 2, we have  $\theta = 90^{\circ}$ ) for different  $M_s$ .

records the fractional change when we vary the  $\theta$ :

$$X = \frac{\sigma(\theta) - \sigma(\theta = 90^{\circ})}{\sigma(\theta = 90^{\circ})},$$
(13)

which evaluates the relative changes of the dispersion compared to the value we have in Figure 2. If the quantity X is small for  $\nabla I'$  and  $\nabla C$  and is not a function of  $M_s$  (see Section 2.4), then we expect that the shape of Figure 2 should remain unchanged. The left and right panels of Figure 3 show how the fractional change is correlated to the relative angle  $\theta$  for our simulations for intensity gradient amplitude dispersion  $\sigma_{\nabla I'}$  and centroid gradient amplitude dispersion  $\sigma_{\nabla C}$ , respectively. We can see that the fractional change is generally on the order of 0.1 and has no visually recognizable trend as a function of  $M_s$ . With these fluctuations we reported that the power law that we see in Figure 2 with  $\theta = 90^{\circ}$  is still seen for other choices of  $\theta$ . From the argument above, we therefore conclude that the effect of  $\theta$  on the power law that we discussed in Figure 2 is not significant.

# 5.2. Test on the Noise Sensitivity

One of the biggest potential discrepancies of the gradient amplitude method is the noise. In the previous development of VGT, the noise is tackled by either a global Gaussian kernel or a low-pass Fourier filter (see Lazarian et al. 2017). For the purpose of tackling the orientation of gradients these methods worked well and have been applied to observations (e.g., Hu et al. 2019b, 2019c). We here would like to test whether the same strategy works for the gradient amplitude method.

We pick the intensity map of the cube "h0-1600" as an example. We gradually add a Gaussian-model white noise to the intensity map with the strength set to be some factor relative to the dispersion of the intensity map. The strength of the noise compared to the dispersion of the intensity map is simply the noise-to-signal ratio (N/S). Since a general practice in observation is to exempt data that have S/N < 3, we would therefore only keep adding white noise up to N/S < 1/3. We would then smooth with Gaussian filters with different width

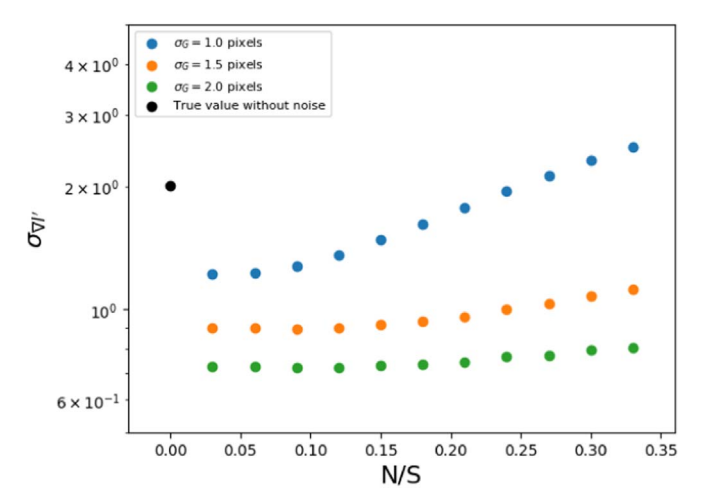
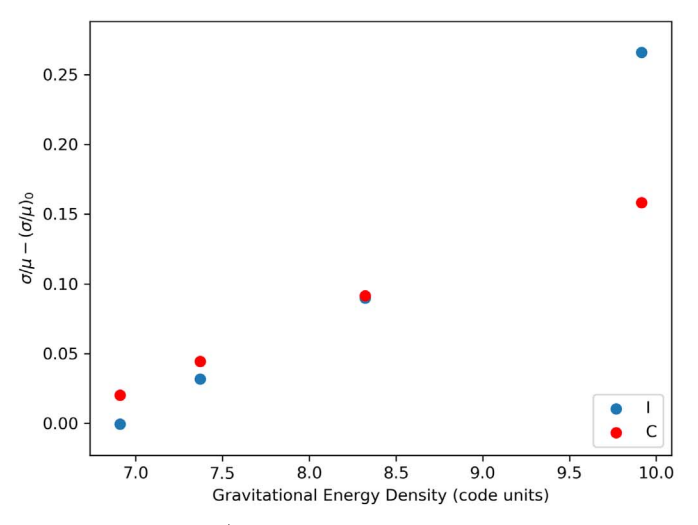


**Figure 4.** Response of  $\sigma_{\nabla l'}$  with respect to the N/S under different Gaussian smoothing kernels (in pixels).

 $\sigma_G$  in units of pixels. Figure 4 shows how the  $\sigma_{\nabla I'}$  responds to the noise levels as we change the size of the Gaussian filter. We could see that when  $\sigma_G$  arrives at 4 pixels, there are simply no recognizable fluctuations for  $\sigma_{\nabla I'}$  as N/S increases. We therefore believe that noise would not be a concern for the intensity gradient amplitude method.

# 6. Determining the Stage of Collapse Using the Gradient Amplitude Statistics

It has been suggested that in the stage of gravitational collapse gradients of intensities and centroids would turn from being perpendicular to magnetic field to parallel *gradually* (Yuen & Lazarian 2017b; Lazarian & Yuen 2018a), which was termed "re-rotation." The concept of re-rotation was applied to recent analysis of observations by Hu et al. (2019b, 2019c). However, the practical procedure of re-rotation still requires further studies. Here we have to be cautious that we are not discussing the statistics of gradient relative orientation to magnetic field (Soler et al. 2013; see also Hu et al. 2019a for a comparison) as a function of column density, but by measuring the differences of the velocity gradient orientation in diffuse



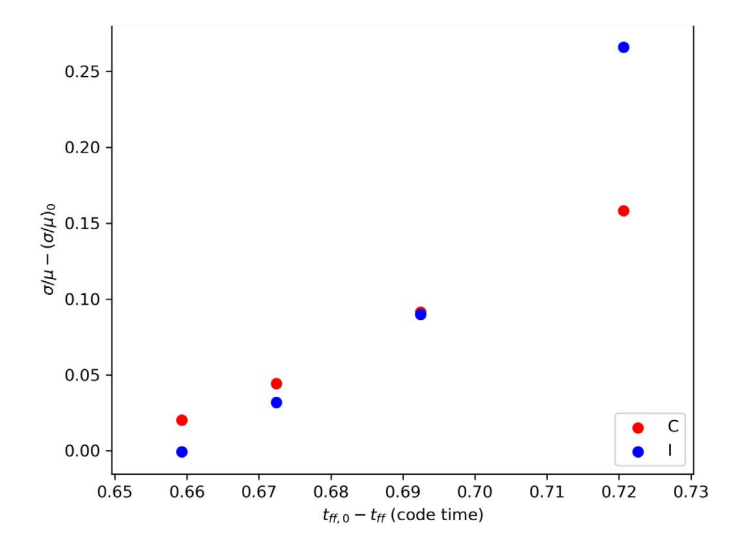


Figure 5. Response of  $\sigma/\mu$  with two commonly used physical parameters measuring the stage of collapse:  $\sigma/\mu$  as a function of the gravitational energy density (left) and relative freefall time (right), for both intensity and centroid.

media and self-gravitating cores as a means of determining the direction of magnetic field without using polarimetry.

Aside from the change of orientations, we should also expect changes of the amplitude of gradients in different stages of gravitational collapse. It is natural that the amplitude of gradients for both densities and velocities would increase owing to the acceleration of gravitational field. Yet such a signature could be possibly confused by strong compressions from shocks. MHD theory tells us that the maximal density enhancement for shock is bounded by either the sonic or the Alfvénic Mach number, depending on the plasma  $\beta$  (Xu et al. 2019). Comparatively, the density enhancement from gravitational collapse is unbounded. When we compute the amplitude of gradient with respect to the ambient mean value, one could possibly see an exponential growth of the gradient amplitude of observables in the self-gravitating region but not the case for shocks. By using numerical simulations to enumerate the collapse of interstellar media, we could test how gradient amplitude would aid in determining the stage of collapse. To investigate the effects of gravity, we evolve the numerical cube h0 to the stage until the high-density structure is not resolvable, which is named the Truelove-Jeans criterion (Truelove et al. 1997).

We use two frequently used physical parameters to characterize the stage of the collapse. The first one is the average gravitational energy density  $\epsilon_{\rm ge} = \langle -\rho \Phi \rangle$ , which is a simple estimate of how clumpy the density structure is when responding to the gravitational field. Notice that in our periodic simulations  $\langle \Phi \rangle = 0$  and  $\langle \rho \rangle = {\rm const}$  guaranteed in all times. The other parameter that is related to the stage of collapse is the relative freefall time  $t_{\rm rff}$ , which is a measure of how long the system has been collapsed since gravity is switched on in our numerical simulation (See Section 3). We compute the freefall time for those pixels having a negative gravitational potential and compare to the freefall time assuming that the whole system is going to collapse, i.e.,  $t_{\rm ff,0} \sim (G \langle \rho \rangle)^{-1/2}$ :

$$t_{\rm rff} = t_{\rm ff,0} - t_{\rm ff}$$
$$\sim (G\langle \rho \rangle)^{-1/2} - (G\langle \rho \rangle_{\Phi < 0})^{-1/2}. \tag{14}$$

The difference between them indicates the time that the collapse has taken. From our discussion, we expect that the part

of the region that has gravitational collapse will have a higher density value, while the ambient environment would have a lower one, which apparently suggests that we should use the dispersion of gradient amplitudes to measure the effect of gravity. However, that could not be used directly because the enhancement of density by gravity is also a function of density. We therefore would compute the parameter  $\sigma/\mu$ , which would normalize the dispersion quantity, hopefully reducing the density contribution from the growth of gradient amplitude.

Figure 5 shows the response of  $\sigma/\mu$  with respect to  $\epsilon_{\rm ge}$  and  $t_{\rm rff}$  for both intensity and centroid gradient amplitudes. We see that there is a linear relationship between  $\sigma/\mu$  and  $\nabla I'$ . We fit the linear relation and see that

$$\left(\frac{\sigma}{\mu}\right)_{I} \approx -0.62 + 0.09\epsilon_{ge}$$

$$\left(\frac{\sigma}{\mu}\right)_{I} \approx -2.89 + 4.35t_{rff}$$
(15)

with  $R^2 > 0.9$ , which gives some insight into the stage of the gravitational collapse when one investigates the gradient amplitude statistics in self-gravitating media. For instance, Hu et al. (2019c) provide a number of clouds with a strong signature of gravitational collapse as indicated by VGT. With our technique we can investigate quantitatively how strong the gravitational collapse is in terms of freefall timescales or gravitational energy density, which can possibly provide the probability of star formation in a given region.

# 7. Deconvolution of Velocity Channel Map

The sonic number not only could possibly help observers characterize the physical conditions of turbulence in molecular clouds but also allows observers to extract the statistics of turbulence in velocity channel maps (see Section 8.1 for the discussions of the strength and caveats of our method). In fact, velocity channels are one of the main observables in the series of VGT papers (Yuen & Lazarian 2017b; Lazarian & Yuen 2018a; Lazarian et al. 2018), and their gradients have been shown to be better in tracing magnetic field directions

compared to the gradients of intensity and centroid maps both numerically (e.g., Lazarian & Yuen 2018a) and observationally (e.g., Hu et al. 2019b, 2019c). Aside from magnetic field tracing, techniques such as velocity channel analysis (VCA) and velocity coordinate spectrum (VCS; Lazarian & Pogosyan 2000; see also their work in Lazarian & Pogosyan 2004, 2006, 2008) also use the statistics of velocity channel maps to predict the three-dimensional velocity and density spectrum from observation.

Lazarian & Pogosyan (2000) suggest that, in the absence of thermal broadening, when the velocity channel is thin, i.e., the velocity window width of the velocity channel is smaller than the characteristic velocity in the velocity channel, the fluctuation of velocity channels is dominated by velocity fluctuations if the 3D density spectrum is steep ( $n_{\rho} < -3$ ). In finite temperature T, the effect of velocity dominance in the velocity channel map is called "velocity crowding." The velocity crowding effect modifies intensity enhancements in channel maps and also flattens the power spectrum of velocity channels.

Since we have shown in Section 4 that intensity and centroid gradient amplitude maps have similar power-law dependencies to  $M_s$  as predicted under the Goldreich & Sridhar (1995) framework, it is very natural to imagine that the same argument as in Section 2 would apply also to the velocity channel map. However, in the presence of strong thermal broadening  $(M_s \ll 1)$ , the channel map is effectively a weighted integral of the intensity map, and thus the velocity channel map gradient amplitude in such a limit would have the same  $M_s$ dependence as their integrated intensity counterpart even through Lazarian & Pogosyan (2000) already formulated analytically how thermal broadening would alter the channel map. The thermal broadening is important for light species, especially for H I and H $\alpha$  lines. For them the corresponding masking of the velocity crowding effect via thermal broadening prevents the proper use of VCA and VCS techniques.

A workaround for such a problem would be to remove the thermal broadening effect from the velocity channel maps. Such a method is possible since thermal broadening is simply a Gaussian convolution with  $c_s$  as the broadening width. The estimation of  $c_s$  is not easy. However, since the thin channels and the thermally broadened thin channels follow statistics derived by Lazarian & Pogosyan (2000), it is possible for us to recognize such a transition by performing the Wiener deconvolution algorithm through a list of trial  $c_s$  even in the presence of noise. We shall see in Section 7.1 how such mathematical constructions would allow us to retrieve  $c_s$ . In the isothermal limit, if we have an estimation of  $M_s$  as listed in Section 4, with the measured spectral line width one could possibly acquire also the injection velocity  $v_L = M_s c_s$ , which is one of the central physical quantities determining the properties of turbulence. In Section 7.1 we would discuss the necessarily mathematical foundations of PPV thermal broadening and the method of deconvolution. In Section 7.2 we discuss how to obtain  $c_s$  by a self-consistent algorithm, and in Section 7.3 we illustrate how the measured  $c_s$  could allow one to reverse engineer the PPV cube without thermal contributions.

# 7.1. Mathematical Formulation on Thermal Broadening and Deconvolution

Mathematically, the density in PPV space of emitters with local sonic speed  $c_s(\mathbf{x}) = \sqrt{\gamma k_B T / \mu_{\text{MMW}}}$ , where  $\mu_{\text{MMW}}$  is the

mean molecular weight of the emitter, moving along the line of sight with stochastic turbulent velocity u(x) and regular coherent velocity, e.g., the galactic shear velocity,  $v_g(x)$ , is (Lazarian & Pogosyan 2004)

$$\rho_s(\boldsymbol{X}, v) = \int_0^S dz \frac{\rho(\boldsymbol{x})}{\sqrt{2\pi\beta_T}} \exp\left[-\frac{(v - v_g(\boldsymbol{x}) - u(\boldsymbol{x}))^2}{2c_s(\boldsymbol{X}, z)^2}\right],$$
(16)

where sky position is described by 2D vector X = (x, y), z is the line-of-sight coordinate, and  $\gamma$  is the adiabatic index. Notice that  $c_s$  would be a function of distance if the emitter is not isothermal. Equation (16) is *exact*, including the case when the temperature of emitters varies in space. The observed velocity channel at velocity position  $v_0$  and channel width  $\Delta v$  is then, assuming a constant velocity window W(v) = 1,

$$Ch(X; \nu_0, \Delta \nu) = \int_{\nu_0 - \Delta \nu/2}^{\nu_0 + \Delta \nu/2} d\nu \rho_s(X, \nu) 
= \int_0^S dz \frac{\rho(x)}{\sqrt{2\pi c_s^2}} \int_{\nu_0 - \Delta \nu/2}^{\nu_0 + \Delta \nu/2} d\nu e^{-\frac{(\nu - \nu_g(x) - u(x)^2}{2c_s^2}}.$$
(17)

Equation (16) represents the effect of the velocity-dependent mapping from the three-dimensional position–position–position (PPP) space to PPV space. Due to this mapping, the PPV density  $\rho_s(X, v)$  at a given velocity v is determined by both the spatial density of the emitters  $\rho(x, y, z)$  and their respective line-of-sight velocities. Note that formal caustics, understood as singularities of a differentiable map from PPP to PPV space, arise only in the limit of  $c_s \rightarrow 0$ .

Equation (16) can be inverted if  $c_s$  is known. We can then connect the thermally broadened PPV cube density  $\rho_s(X, \nu)$  to that of the underlying PPV density  $\rho_v(X, \nu)$ :

$$\rho_{s}(X, v) = \int dv' \rho_{v}(X, v') e^{-\frac{(v-v')^{2}}{2c_{s}^{2}}},$$
 (18)

which is a convolution of the raw PPV density  $\rho_{\nu}(X, \nu)$  with respect to the thermal Gaussian kernel  $G(\nu) = \frac{1}{\sqrt{2\pi c_s^2}} \exp\left(-\frac{\nu^2}{2c_s^2(X)}\right)$ , a function of the sonic speed.

# 7.2. Mapping c<sub>s</sub> by Constructing Exponential Reduced Centroids

We consider the following integral:

$$\rho_{e}(X, v) = \frac{\int_{|v| > \sqrt{2} c_{s}'} dv' \rho_{s}(X, v') e^{+\frac{(v-v')^{2}}{2c_{s}^{2}}}}{\int_{|v| > \sqrt{2} c_{s}'} e^{+\frac{(v-v')^{2}}{2c_{s}^{2}}}},$$
(19)

which integrates the observed PPV density  $\rho_s(X, v')$  with an exponential factor that looks like the inverse convolution of the Gaussian kernel G(v), which we term the exponential reduced centroid (ERC). However, we must remind the reader that the expression in Equation (19) is not a deconvolution of the thermal function.

To perform the study numerically, we prepared a series of synthetic PPV densities by using the PPV cube of h0-1200 and convolved the simulations with different values  $c_s$  in the range of  $0.25c_{s,\text{actual}} - 10.0c_{s,\text{actual}}$ , where  $c_{s,\text{actual}}$  is the actual value we put into the simulation. We then compute the ERC function following Equation (19). We show pictorially how the ERC

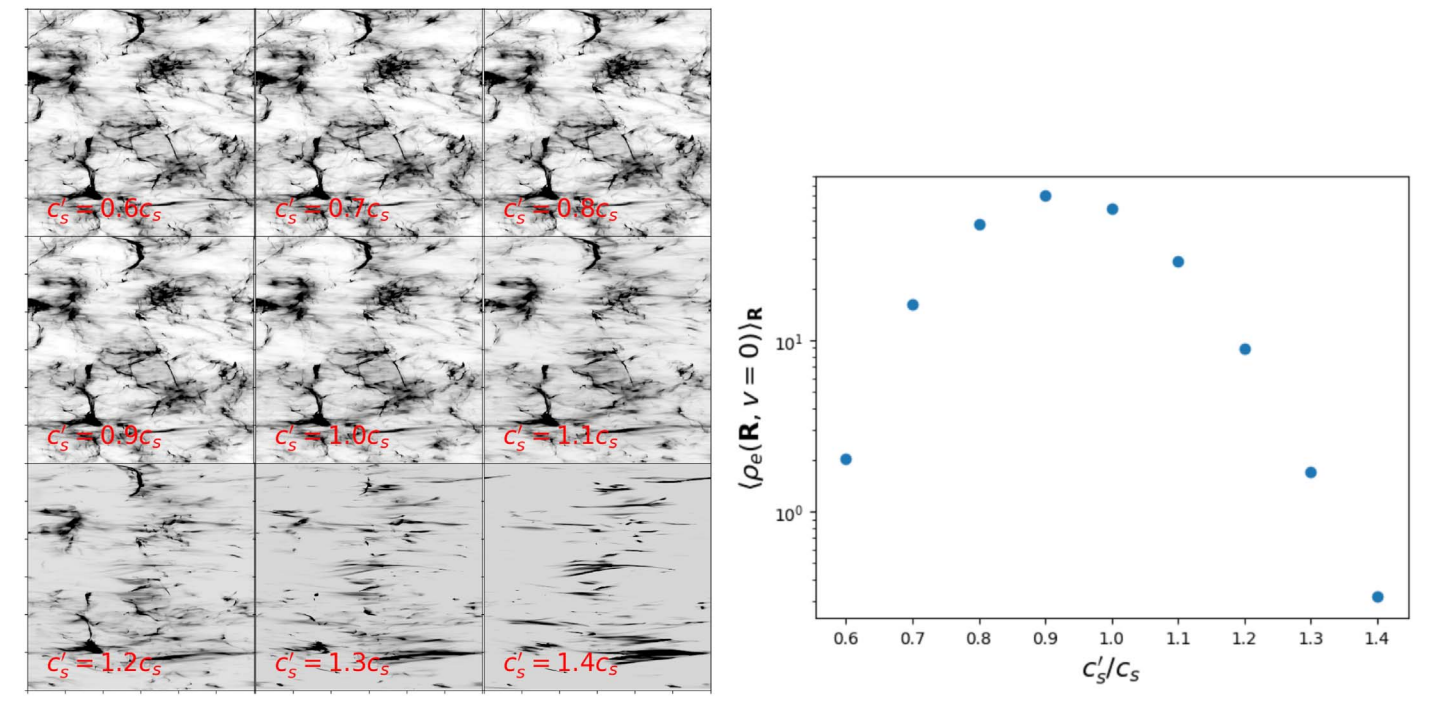


Figure 6. Left: set of illustrative figures showing how the ERC would behave as a function of prior  $c_s'$ . The color bar scale is relative for all maps and set similarly to Figure 1. Right: mean amplitude of the ERC as a function of  $c_s'/c_s$ .

behaves in the left panel of Figure 6 as we vary our guess of  $c_s'$ . When  $c_s'$  is small, the ERC is actually intensity-like (readers could compare the results from Figure 6 to those in Figure 7), meaning that the cross-correlation between the ERC and intensity map is high. When  $c_s'$  is large, the ERC becomes velocity like and has obvious striations that are not from the density structures. The right panel of Figure 6 shows how the mean amplitude of the ERC  $\rho_e(X, v')$  behaves as a function of  $c_s'/c_s$ . We see that the mean amplitude of the ERC follows the special property that it peaks at around  $c_s'/c_s \sim 1$  (exact value: 0.9). We see this property around different settings on  $c_s'$  and  $c_s$ , and we believe that this provides a unique way to probe the sonic speed.

# 7.3. Wiener Deconvolution Algorithm

Since we already obtained an estimate of  $c_s$  from the previous subsection, we can thus deconvolve the raw PPV density  $\rho_v(X, v)$  from the observed PPV cube  $\rho_s(X, v)$ . Assuming that we have a prediction of sonic speed  $c_s'$  (which might be different from true sonic speed  $c_s$ ), we see that the Wiener deconvolution algorithm would allow us to estimate the underlying PPV density  $\rho_v'$  if the N/S is provided:

$$\mathcal{F}\{\rho_{v}'\} = \frac{\mathcal{F}\{G(c_{s}')\} \cdot \mathcal{F}\{\rho_{s}\}}{|\mathcal{F}\{G(c_{s}')\}|^{2} + (N/S)^{2}},$$
(20)

where  $\mathcal{F}$  is the Fourier transform operator and N/S is the noise-to-signal ratio. In other words, the actual primitive PPV density  $\rho_v$  and the estimated PPV density  $\rho_v$  would be related by

$$\mathcal{F}\{\rho_{v}'\} = \mathcal{F}\{\rho_{v}\} \frac{2\pi c_{s} c_{s}' e^{-2\pi k^{2} (c_{s}^{2} + c_{s}'^{2})}}{e^{-4\pi k^{2} c_{s}'^{2}} + (N/S)^{2}}.$$
 (21)

Figure 8 shows how the algorithm deconvolves the PPV cube in the presence of noise and the variation of  $c_s$ . One could

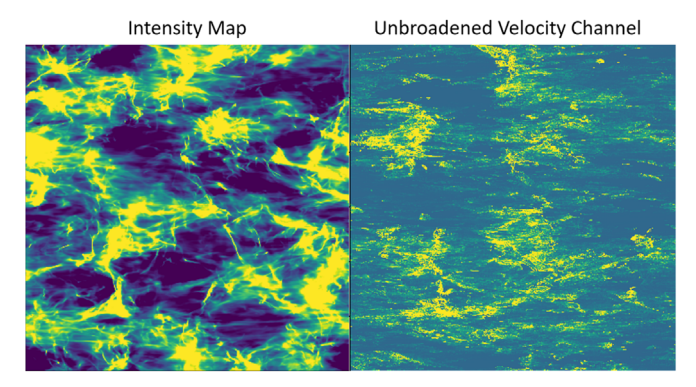


**Figure 7.** Intensity and velocity channel of the cube h0-1200 when we set  $c_s = 10c_{s,actual}$ .

see that when  $c_s' < c_s$ , the map is basically noise-like and has a power spectrum with positive slope. When  $c_s' > c_s$ , the structure of the velocity channel map would be similar to that we show in the left panel of Figure 7. Only when we choose an appropriate  $c_s' \sim c_s$ , which could be recognized by spectral slopes, could one see velocity-like structures like those we displayed in the right panel of Figure 7.

### 8. Discussions

# 8.1. Importance, Possible Future Studies, and Caveats of Our Work

Our work here focuses on obtaining two of the most important astrophysical quantities based on the amplitude statistics of the observables, namely, the sonic Mach number (Sections 2, 4) and the sonic speed (Section 7). We start from theory that there should be an expected correlation between the observed intensity gradient amplitude and the underlying sonic Mach number, which we also confirm numerically. As a separate development, the sonic speed is obtained by probing

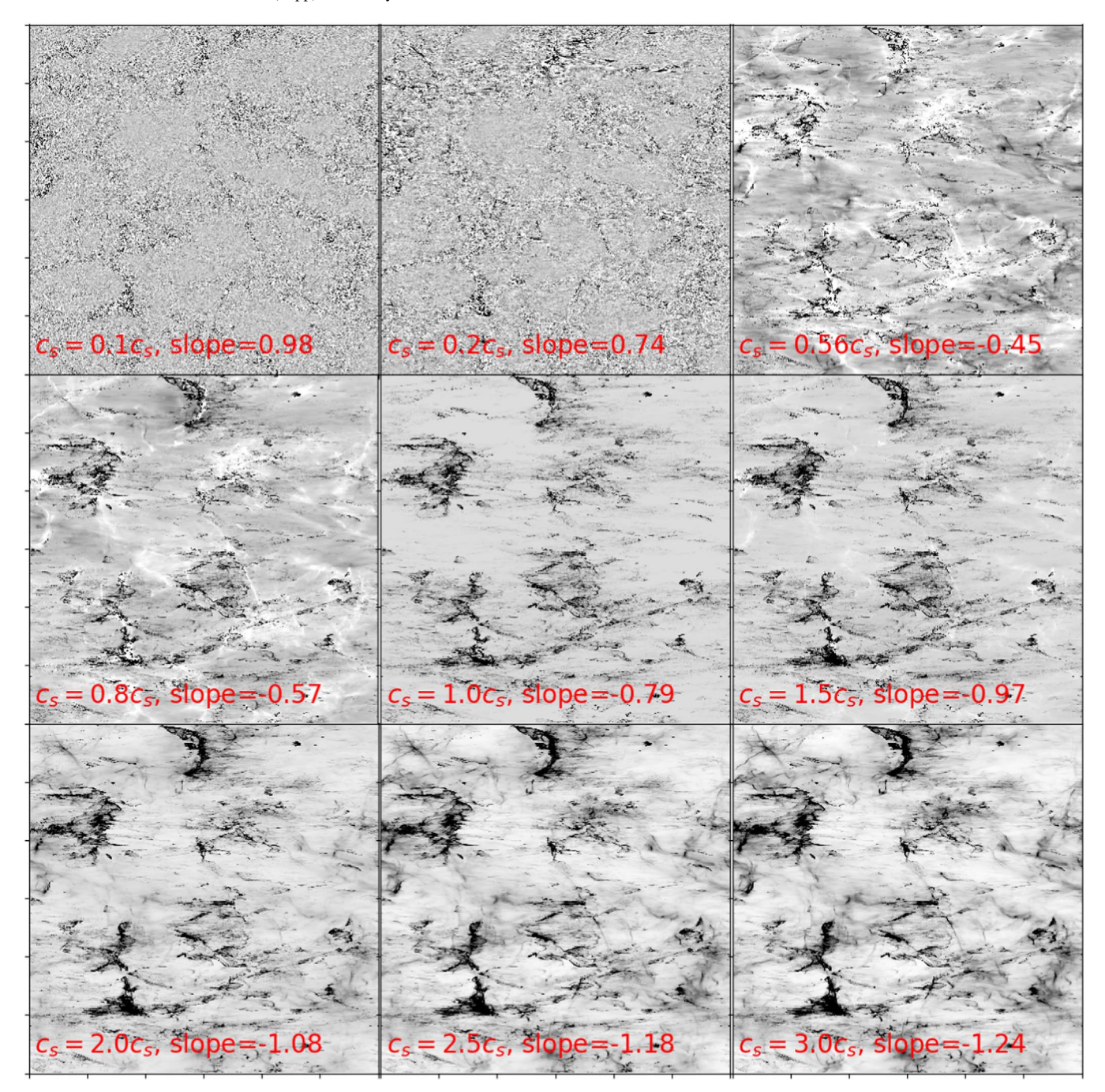


Figure 8. Deconvolved PPV cube at v = 0, i.e.,  $\rho_v(\mathbf{R}, v = 0)$  as a function of  $c_s^{\prime}/c_s$ , with the label including the spectral slopes.

the mean amplitude of the exponential reduced centroid, which allows us to estimate not only the injection velocity  $v_L = M_s c_s$  but also the true, thermally unbroadened PPV cube (Section 7.3). The power of amplitude statistics with the support of the theory of MHD turbulence (Goldreich & Sridhar 1995; Lazarian & Vishniac 1999; Cho & Lazarian 2003) and observational diagnostics (Lazarian & Pogosyan 2000, 2004, 2006) provides a unique way to probe the physical conditions and extract turbulence statistics in observed spectroscopic data. Moreover, with the PPV cube without thermal broadening, we can safely use the tools developed from Lazarian & Pogosyan (2000, 2004) about the statistics of turbulence both parallel and perpendicular to the line of sight. This shows that the amplitude statistics has its unique position

in predicting the turbulence statistics, and could possibly be used in situations that have more physics involved, e.g., multiphase media and gravito-magnetohydrodynamics.

One of the small but very important aspects is the constant dependence of velocity gradient amplitudes on both sonic and Alfvénic Mach number as when  $M_s \gg 1$ . This constancy is expected from theory, but currently we cannot possibly apply it to observations since we do not observe the pure velocity map from spectroscopic data. This should be further studied both theoretically and numerically. The theory that we derived in Section 2 depends also on the mode composition in the astrophysical turbulence, which is also a quantity that has no easy option to obtain. While there are attempts (Zhang et al. 2020; Makwana & Yan 2019; Chepurnov & Lazarian 2010) in

acquiring them both numerically and based on the observed synchrotron data, such a method is not extended to the regime that we are tackling now. Due to the differences of the dependence of the  $M_s$  and  $M_A$  for the three different modes, it is possible to use gradient amplitude as a quantifier to estimate the relative weights of the modes, or at least the ratio between compressible and incompressible modes. We could see from Table 1 that, in the case of sub-Alfvénic systems, there is a dependence on  $M_A$  for Alfvén modes but not for the two compressible modes. Measuring the value of  $M_A$  could probably allow us to estimate the ratio of the modes since the variance of the gradient amplitudes from different modes is contributed by the squared sum of their respective dispersions. By modeling this, we should be able to obtain the ratio of modes.

One of the very important caveats here that requires further study is the existence of the rotation curve. In our discussion in Section 7 we do not take the effect of galactic shear into account since we would like to simplify our deviation. However, for applications to large-scale data like the H I maps, it is necessary to also consider the effect of galactic rotation. Fortunately, this could be possibly studied both numerically and observationally by introducing a proper rotation curve model that corresponds to our Galaxy. The quality of the wing channel is also a concern in the method of Section 7, since if there is only a limited number of the channels provided, the deconvolution algorithm might not have enough data in acquiring the PPV cube. Another caveat in the gradient amplitude is that there does exist a variation of intensity gradient amplitude statistics due to the different weighting of modes and the line-of-sight effects, which are both hard to estimate in observations. Comparatively, the centroid gradient amplitude would be more robust in terms of real application if one could accept  $\sigma_{\nabla C} \sim M_s^{\alpha}$  with  $1 < \alpha < 2$  as acquired in Figure 2.

# 8.2. Importance to the Development of MHD Turbulence Theory and Interactions between Theory and Observations

We discussed in Section 2 that the whole idea of applying GS95 to real-life astrophysical observations is to have some sort of statistical averaging on some MHD variables, with proper estimations on the observational effects. For example, one should consider the effect of projections if the observable is obtained by some other variables collected along line of sight. If a velocity axis exists along the line of sight, then it is important to understand how the velocity effect contributes to the observable. The statistical averaging, though implicitly applied, could actually be found in a vast number of literature, for instance, the use of spectra (Maron & Goldreich 2001), velocity-distance relation (Larson 1981), correlation and structure functions (Esquivel & Lazarian 2005), histogram of orientations (Soler et al. 2013), and block averaging (Yuen & Lazarian 2017a). The current work uses the same principle as the same author did 3 yr ago in Yuen & Lazarian (2017a). The same idea has been brought to here by simply using the mean (Section 7.1) and the dispersion (Section 2.4) of the observables. It is expected that the theory could predict with observations better by testing which statistical quantifier would be the best in extracting the statistical behavior from the observables based on the GS95 scaling.

# 8.3. Implications to the Development of the Velocity Gradient Technique

The VGT in its current form provides a reliable way of tracing magnetic field directions. Our work here is the first attempt to connect the *gradient amplitudes* to  $M_s$  and quantify their relation through the same principle that formulates VGT. We note that the visual correspondence that we demonstrated is also handy for observers to approximate the physical conditions in the parts of the ISM. The prospect of using gradients to probe physical conditions further increases the value of the VGT by helping to further constrain the physical conditions in different ISM phases. We expect that this should help in choosing between different models of star formation (see Crutcher et al. 2010; Crutcher 2012; Lazarian et al. 2012).

This work provides the values of  $M_s$  in a cost-effective way and complementary to other papers on VGT targeting Mach numbers, e.g., Lazarian et al. (2018) use dispersion of velocity gradients to estimate  $M_A$ . Synergistic use of these methods provides a way to cross-check the measurements. Moreover, in cases when polarimetry data are unavailable, the gradient technique provides an alternative way to study the physical conditions of interstellar media.

### 8.4. Role of Thermal Broadening

The VGT has become a sophisticated technique applicable to studying both subsonic and supersonic environments. For probing VGT for subsonic turbulence in practice, one can use different approaches. First of all, the velocity centroids are not contaminated by thermal broadening (see Esquivel & Lazarian 2005; Kandel et al. 2016), and therefore the centroid gradients can be used if the thermal broadening exceeds the turbulent one. Reduced centroids (Lazarian & Yuen 2018a) can be applied to the spectral line data broadened by galactic rotation.

Channel maps provide a valuable way of analyzing the data. In the case of H I, it was noted in Lazarian & Pogsyan (2000) that while the warm H I may dominate at high galactic latitudes in terms of total emissivity, the contribution from cold H I is expected still to dominate in thin channels. Therefore, if the current view of the two-phase turbulent H I, namely, clumps of cold H I moved together and by the warm H I, is true, the statistics of thin channels represents the statistics of velocity with cold H I serving as a tracer of the warm H I dynamics. This is explained in more detail in Yuen et al. (2019).

This paper, however, discusses a way to deal with the thermal broadening through the deconvolution. This approach can be useful for, e.g.,  $H\alpha$  emission lines. While Lazarian & Pogosyan (2000) showed that the thermal line widths act as broad channels, the effect of thermal broadening is pretty simple in terms of its statistics. This allows the procedure of deconvolution that we demonstrated in this paper.

# 8.5. Applying the Results to Various Spectral Lines

Our study follows the empirical approach to obtaining the sonic Mach number that was explored in earlier papers (see Burkhart & Lazarian 2012). The difference is that we use amplitudes of the gradients of velocity centroids. Our technique does not depend on the interpretation of 21 cm intensity enhancements in thin channel maps that has been debated recently (see Clark et al. 2019; Yuen et al. 2019). Moreover, H I is only one type of media to which the application of the

technique is sought. Other optically thin lines, e.g., C18O, can be used. In analogy with the earlier studies exploring the effects of optical depth on the gradient technique (González-Casanova et al. 2019; Hsieh et al. 2019; Hu et al. 2019b), we expect that our present results can be applicable to CO lines with a moderate amount of self-absorption, e.g., <sup>13</sup>CO lines. The corresponding study of different lines will be provided elsewhere.

The additional information obtained by the gradient amplitude method is handy within the gradient technique. The accuracy of the gradient technique in tracing magnetic field depends on the sonic Alfvén Mach number  $M_s$ . In particular, the density enhancements associated with shocks can affect the intensity gradients. The increase of the amplitude of the gradients can help identify shocks. The marginal dependence of the gradient amplitudes on the media magnetization and angle between the magnetic field and line of sight makes the present technique of studying  $M_s$  rather robust. This testifies to the importance of our suggested technique of identifying  $M_s$ .

### 9. Conclusions

In this work, we explore how the amplitude statistics would help explore the properties of interstellar turbulence through two aspects: the gradient amplitudes and the removal of thermal broadening. To summarize:

- 1. Based on the theory of MHD turbulence (Section 2), we derive a set of formulae for the amplitudes of three-dimensional velocities (Sections 2.1, 2.2) and densities (Section 2.3) for their dependencies on sonic and Alfvénic mach number, as well as the dependencies on modes (Table 1).
- 2. We also derive similar predictions in gradient amplitudes of observables and discuss how to use them in observations (Section 2.4).
- 3. We tested our prediction in MHD simulations with simple statistical parameters (Section 4).
- 4. We show that our prediction is robust to noise as long as a suitable Gaussian kernel is used (Section 5).
- 5. We discuss the potential use of the amplitude method in a self-gravitating system (Section 6).
- 6. We discuss how the adoption of the amplitude method can help in deconvolving the observed velocity channel with strong thermal contamination (Section 7).

We acknowledge Yue Hu and Ka Wai Ho for the fruitful discussions, as well as the hospitality of the University of California, Santa Barbara, in the summer of 2019. We acknowledge the support of NSF AST 1816234 and NASA TCAN 144AAG1967. This research used resources of the National Energy Research Scientific Computing Center (NERSC), a U.S. Department of Energy Office of Science User Facility operated under contract No. DE-AC02-05CH11231, as allocated by TCAN 144AAG1967.

# Appendix Extending to Nonisothermal Systems

The aforementioned analysis focuses on the relation of the gradient amplitude to the sonic Mach number in the case of isothermal environments. For the isothermal simulations we employed in the main text, since the computation does not involve a definite length scale (e.g., involvement of gravitational

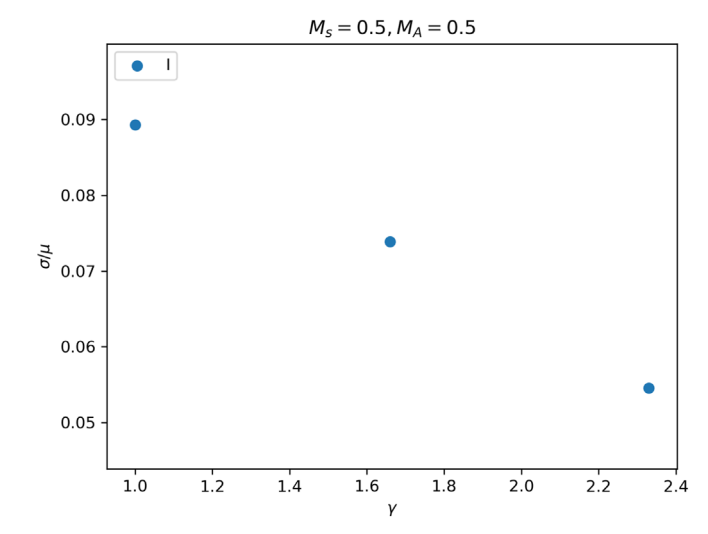


**Figure A1.** Change of  $\sigma/\mu$  with respect to the polytropic index  $\gamma$  in adiabatic systems with the polytropic equation of state  $P \propto \rho^{\gamma}$  and  $M_s$ ,  $M_A = 0.5$ .

Table A1

Description of Adiabatic MHD Simulation Cubes, Some of Which Have Been

Used in the Series of Papers about VGT (Yuen & Lazarian 2017a, 2017b;

Lazarian & Yuen 2018a, 2018b)

Model	$M_S$	$M_{\rm A}$	$\beta = 2M_{\rm A}^2/M_{\rm S}^2$	Resolution
Adiabatic $\gamma = 1.00$	0.50	0.50	2.00	640 <sup>3</sup>
Adiabatic $\gamma = 1.67$	0.50	0.50	2.00	$640^{3}$
Adiabatic $\gamma = 2.33$	0.50	0.50	2.00	$640^{3}$

**Note.**  $M_s$  and  $M_A$  are the rms values at each snapshot.

length scale), therefore the only parameters that determine the saturated simulations are  $M_s$ ,  $M_A$  and the box length scale L. These simulations are scale-free and can be rescaled to other units to compare with observations.

However, in the case of diffuse interstellar media, where a distinct equation of state plus gas heating and cooling become important in understanding the dynamics and structure formations within the ISM, we should expect the amplitude of gradients to behave differently from the isothermal counterpart, for instance, in the case of adiabatic conditions for H I, where  $P \propto \rho^{5/3}$  (See Kritsuk et al. 2017, 2018). In the case of phase equilibrium, the warm and cold neutral media can both be modeled by an adiabatic equation of state (see also Wolfire et al. 1995 and references therein); the pressure exerted due to the crowding of density is larger than its counterpart in the isothermal system. As a result, the gas tends to have a smaller density (or intensity, in observation) gradient amplitude. While it is true that the isothermal condition is generally true for giant molecular clouds, such an assumption is not correct for HI. Therefore, there is a need for us to understand how the theory of gradient amplitude changes in the case of nonisothermal environments.

We test the result of gradient amplitude using the adiabatic numerical simulations in Table A1 and plot the  $\sigma/\mu$  against polytropic index  $\gamma$  in Figure A1. We see that when  $\gamma$  increases,  $\sigma/\mu$  drops significantly.

### References

Armstrong, J. W., Rickett, B. J., & Spangler, S. R. 1995, ApJ, 443, 209 Begum, A., Chengalur, J. N., & Bhardwaj, S. 2006, MNRAS, 372, L33

```
Beresnyak, A., & Lazarian, A. 2019, Turbulence in Magnetohydrodynamics
   (Berlin: De Gruyter)
Beresnyak, A., Lazarian, A., & Cho, J. 2005, ApJL, 624, L93
Biskamp, D. 2003, Magnetohydrodynamic Turbulence (Cambridge:
   Cambridge Univ. Press), 310
Brandenburg, A., & Lazarian, A. 2013, SSRv, 178, 163
Burkhart, B., & Lazarian, A. 2012, ApJL, 755, L19
Burkhart, B., Lazarian, A., Leão, I. C., de Medeiros, J. R., & Esquivel, A.
   2014, ApJ, 790, 130
Chepurnov, A., & Lazarian, A. 2010, ApJ, 710, 853
Cho, J., & Lazarian, A. 2002, PhRvL, 88, 245001
Cho, J., & Lazarian, A. 2003, MNRAS, 345, 325
Cho, J., & Lazarian, A. 2006, ApJ, 638, 811
Cho, J., & Vishniac, E. T. 2000, ApJ, 539, 273
Clark, S. E., Peek, J. E. G., & Miville-Deschenes, M.-A. 2019, ApJ, 874, 171
Crutcher, R. M. 2012, ARA&A, 50, 29
Crutcher, R. M., Hakobian, N., & Troland, T. H. 2010, MNRAS, 402, L64
Deshpande, A. A., Dwarakanath, K. S., & Goss, W. M. 2000, ApJ, 543, 227
Dickey, J. M., McClure-Griffiths, N. M., Stanimirović, S., Gaensler, B. M., &
   Green, A. J. 2001, ApJ, 561, 264
Draine, B. T. 2009, in ASP Conf. Ser. 414, Cosmic Dust—Near and Far, ed.
   T. Henning, E. Grün, & J. Steinacker (San Francisco, CA: ASP), 453
Elmegreen, B. G., & Scalo, J. 2004, ARA&A, 42, 211
Esquivel, A., & Lazarian, A. 2005, ApJ, 631, 320
Federrath, C., Roman-Duval, J., Klessen, R. S., Schmidt, W., &
   Mac Low, M.-M. 2010, A&A, 512, A81
Fissel, L. M., Ade, P. A. R., Angilè, F. E., et al. 2016, ApJ, 824, 134
Goldreich, P., & Sridhar, S. 1995, AJ, 438, 763
González-Casanova, D. F., & Lazarian, A. 2017, ApJ, 835, 41
González-Casanova, D. F., Lazarian, A., & Burkhart, B. 2019, MNRAS,
   483, 1287
Green, D. A. 1993, MNRAS, 262, 327
Heyer, M., Gong, H., Ostriker, E., & Brunt, C. 2008, ApJ, 680, 420
Heyer, M., Krawczyk, C., Duval, J., & Jackson, J. M. 2009, ApJ, 699,
```

Hsieh, C.-. h., Hu, Y., Lai, S. P., et al. 2019, ApJ, 873, 16

Hu, Y., Yuen, K. H., & Lazarian, A. 2019a, ApJ, 886, 17

Jokipii, J. R. 1966, ApJ, 146, 480

Hu, Y., Yuen, K. H., Lazarian, A., et al. 2019b, NatAs, 3, 776

Kandel, D., Lazarian, A., & Pogosyan, D. 2016, MNRAS, 461, 1227

Kandel, D., Lazarian, A., & Pogosyan, D. 2017, MNRAS, 464, 3617

Hu, Y., Yuen, K. H., Lazarian, V., et al. 2019c, ApJ, 886, 17

```
Khalil, A., Joncas, G., Nekka, F., Kestener, P., & Arneodo, A. 2006, ApJS,
  165, 512
Konstandin, L., Girichidis, P., Federrath, C., et al. 2012, ApJ, 761, 149
Kowal, G., & Lazarian, A. 2010, ApJ, 720, 742
Kowal, G., Lazarian, A., & Beresnyak, A. 2007, ApJ, 658, 423
Kowal, G., Lazarian, A., Vishniac, E. T., & Otmianowska-Mazur, K. 2009,
   ApJ, 700, 63
Kritsuk, A. G., Flauger, R., & Ustyugov, S. D. 2018, PhRvL, 121, 021104
Kritsuk, A. G., Ustyugov, S. D., & Norman, M. L. 2017, NJPh, 19, 065003
Larson, R. B. 1981, MNRAS, 194, 809
Lazarian, A. 2006, ApJL, 654, L25
Lazarian, A., & Esquivel, A. 2003, ApJL, 592, L37
Lazarian, A., Esquivel, A., & Crutcher, R. 2012, ApJ, 757, 154
Lazarian, A., & Pogosyan, D. 2000, ApJ, 537, 720
Lazarian, A., & Pogosyan, D. 2004, ApJ, 616, 943
Lazarian, A., & Pogosyan, D. 2006, ApJ, 652, 1348
Lazarian, A., & Pogosyan, D. 2008, ApJ, 686, 350
Lazarian, A., & Vishniac, E. T. 1999, ApJ, 517, 700
Lazarian, A., & Yuen, K. H. 2018a, ApJ, 853, 96
Lazarian, A., & Yuen, K. H. 2018b, ApJ, 865, 59
Lazarian, A., Yuen, K. H., Ho, K. W., et al. 2018, ApJ, 865, 46
Lazarian, A., Yuen, K. H., Lee, H., & Cho, J. 2017, ApJ, 842, 30
Mac Low, M.-M., & Klessen, R. S. 2004, RvMP, 76, 125
Makwana, K. D., & Yan, H. 2019, arXiv:1907.01853
Maron, J., & Goldreich, P. 2001, ApJ, 554, 1175
McKee, C. F., & Ostriker, E. C. 2007, ARA&A, 45, 565
Padoan, P., Juvela, M., Kritsuk, A., & Norman, M. L. 2006, ApJL, 653, L125
Soler, J. D., & Hennebelle, P. 2017, A&A, 607, A2
Soler, J. D., Hennebelle, P., Martin, P. G., et al. 2013, ApJ, 774, 128, ApJ,
  130, 241
Truelove, J. K., Klein, R. I., McKee, C. F., et al. 1997, ApJL, 489, L179
Wolfire, M. G., Hollenbach, D., McKee, C. F., Tielens, A. G. G. M., &
  Bakes, E. L. O. 1995, ApJ, 443, 152
Xu, S., Ji, S., & Lazarian, A. 2019, ApJ, 878, 157
Yan, H., & Lazarian, A. 2008, ApJ, 673, 942
Yuen, K. H., Chen, J., Hu, Y., et al. 2018, ApJ, 865, 54
Yuen, K. H., Hu, Y., Lazarian, A., & Pogosyan, D. 2019, arXiv:1904.03173
Yuen, K. H., & Lazarian, A. 2017a, ApJL, 837, L24
Yuen, K. H., & Lazarian, A. 2017b, arXiv:1703.03026
Yuen, K. H., & Lazarian, A. 2020, ApJ, 898, 66
Zhang, H., Chepurnov, A., Yan, H., et al. 2020, NatAs, in press (doi:10.1038/
  s41550-020-1093-4)
```